ORIGINAL PAPER

XAFS and XRD study on Fe, Ni, and Ge in iron meteorite NWA 859

Huimin Shao[1] · Hiroshi Isobe[1] · Ginga Kitahara[1] · Hiroshi Fukui[2] · Akira Yoshiasa[1]

Abstract

Iron meteorites record the evolutionary and cosmochemical processes of their parent bodies. Fe–Ni phases in iron meteorites show complex textures from various thermal histories of parent bodies as well as the phase relationships and crystal chemistry of Fe–Ni metal. Synchrotron radiation-based X-ray absorption fine structure spectra and X-ray diffraction were applied herein to the study of iron meteorite NWA 859 Fe, Ni, and Ge contents at the K-edge, since they are effective techniques in identifying crystal structures in iron meteorites. The bond distances of Fe and Ni in tetrataenite and kamacite were detected. Field-emission scanning electron microscopy and energy-dispersive spectroscopy were used to observe the petrological and chemical characteristics of the main minerals, kamacite and tetrataenite, and the trace mineral schreibersite. The tetrataenite phase and body-centered cubic kamacite formed a Widmanstätten pattern and cloudy zone. The extended X-ray absorption fine structure (EXAFS) analyses of NWA 859 and a single-crystal diffraction of tetrataenite show that it has a near-face-centered cubic (FCC) tetragonal structure with 12 nearest-neighboring Ni, Fe, and Ge atoms at distances of $r_{Ni-(Ni, Fe)} = 2.5170(13)$ Å, $r_{Fe-(Ni, Fe)} = 2.534(3)$ Å, and $r_{Ge-(Ni, Fe)} = 2.524(5)$ Å, respectively. Moreover, the X-ray absorption near-edge structure (XANES) spectra suggest that the Ge in tetrataenite exhibits a specific local structure with coordination number 12, suggesting that a new local structure of Ge-(Ni, Fe) was first discovered in extraterrestrial material, forming a stable tetragonal structure at approximately 688–618 K. X-ray absorption fine structure (XAFS) is an efficient technique that could provide us further information about local atomic structures and forming conditions in extraterrestrial materials without damage.

Keywords Iron meteorite · XAFS · Local structure · Tetrataenite · Thermal history

Introduction

Iron meteorites are the only natural samples that can be used as an analog material for the Earth's core. In them, the local structure of atoms is essential for exploring the evolutionary and cosmochemical processes of their parent bodies. To interpret the origin of iron meteorite samples and their formation conditions, a series of chemical analyses were conducted, forming a basic chemical classification system (Schaudy et al. 1972; Scott 1972; Wasson 1967, 1970; Wasson and Kimbeblin 1967). These analyses, however, revealed limited information and only covered a chemical scale. With the benefit of instrumental and technological advances, the X-ray absorption fine structure (XAFS) method provides an opportunity to gain insight into the local structure of atoms in iron meteorites. The XAFS method has been applied widely to various elements in diverse materials, even at very low concentrations (Takahashi et al. 2000). The bonding distance between a target atom and its neighbors can be obtained via extended X-ray absorption fine structure (EXAFS) with high precision. As early as 1989, EXAFS has been an effective technique in identifying kamacite–taenite structures in iron meteorites (Cressey et al. 1989).

The size of the iron meteorite parent bodies can be estimated using the cooling rate, which is recorded in the textures and composition of the kamacite and taenite phases that resulted from the phase relations of Fe and Ni metal.

✉ Huimin Shao
huimin_shao1994@163.com

Hiroshi Fukui
fukuih@sci.u-hyogo.ac.jp

[1] Department of Earth and Environmental Sciences, Faculty of Advanced Science and Technology, Kumamoto University, Kumamoto 860-8555, Japan

[2] Department of Material Science, Graduate School of Material Science, University of Hyogo, Hyogo 678-1297, Japan

(Yang et al. 2007). The well-known Widmanstätten pattern of crystallographically oriented kamacite plates in taenite provides detailed information regarding the cooling history based on certain characteristics. Thus, the Fe–Ni phase diagram and phase relationship are well understood.

Germanium can exhibit a crystallographic character that provides information regarding the relationship between Fe and Ni metal. Germanium concentrations in iron meteorites were first quantified by Lovering et al. (1957), showing important chemical behavior during fractionation (Wai and Wasson 1979; Wasson 1970; Wasson and Kimbeblin 1967; Xue et al. 1997). However, the local structure of Ge in iron meteorites is not widely researched. The iron meteorite NWA 859 is chemically related to another iron meteorite, Butler, both of which exhibit plessitic octahedrite structures (Wasson 2011). Furthermore, they show the highest Ge concentration in all known iron meteorites, providing us with the opportunity to observe the local structure of Ge. Wasson (2011) determined that it was unclear if NWA 859 and Butler formed magmatically based on their unclear magmatic trends. Therefore, Wasson proposed that they may be formed as a result of impacts with non-magmatic formation histories (Wasson 2011).

In this study, a series of techniques, including X-ray diffraction (XRD), scanning electron microscope (SEM), energy-dispersive X-ray spectroscopy (EDS), and XAFS spectroscopy, were applied to Fe, Ni, and Ge in the iron meteorite NWA 859 to understand its crystallographic, chemical, and textural properties. The evolution history of iron meteorites was recorded in crystal structure and chemical characteristics. Thus, the events happened in their parent bodies could be inferred from such evidences. Physical cutting of the sample may cause crystallographic distortion of the sample surface. Therefore, chemical etching treatment methods were used for removal of surface layers with potential surface damage and separation of kamacite and tetrataenite phases. The discovered characteristics of the local structure of Fe, Ni, and Ge were then evaluated in combination with the thermal history and the phase relation of Fe–Ni system.

Samples and experimental methods

The sample used in this study is one piece of the iron meteorite NWA 859, which is an ungrouped iron meteorite. It was found in Taza, Morocco, and belongs to the plessitic octahedrite texture group. The sample used herein was cut into 2 mm-thick pieces, and chemical etching was employed to reveal the Widmanstätten pattern.

A field-emission SEM (FE-SEM, JEOL JSM-7001F) equipped with EDS (Oxford Aztec system) was used to observe the microstructure to analyze its chemical composition without a conductive coating. Co was used for optimization for the beam current and standard samples for Fe, Ni, Co, and Ge were Fe_2O_3 and pure metals of Ni, Co, and Ge, respectively. The accelerating voltage and beam current were 15 kV and 1.7 nA, respectively.

Nital etching was conducted for phase separation and to avoid artificial stress. A 3% concentration Nital solution was prepared using high-grade reagents of anhydrous ethanol and nitric acid. The sliced sample size was 1 mm thick, 1 mm wide, and 7 mm long. One piece of the sample was kept in the Nital solution for 24 h, and the other was kept at ambient temperature for 48 h. The completely separated phases were detected using the latter and were analyzed directly. After etching, the sample was observed via SEM and EDS.

Powder diffraction patterns were measured using an X-ray diffractometer (Rigaku, RINT-Ultima3). Cu Kα1 ($\lambda = 1.5408$ Å) was employed, and a slightly etched flat sample surface was set at the sample holder directly. Ni (Chameleon Guaranteed Reagent, Japan) and Fe (Wako Pure Chemical Industries. LTD., Japan) reagents were also measured under 40 kV and 40 mA at steps of 0.5°/min from 40° to 120° 2θ. X-ray diffractograms were compared with a database in the PDXL 2.0 software. Lattice parameters were calculated based on the detected d-spacing and plane indices via the least-squares method.

Single crystals of tetrataenite and schreibersite were carefully selected from the etched sample surface to avoid stress. The determination of the lattice constants and the confirmation of the single crystalline state for tetrataenite and schreibersite were performed using the single-crystal diffraction method. Crystallographic data were collected on a Rigaku SuperNova single source at offset/far, HyPix3000 diffractometer. Then, the Mo X-ray generator ($\lambda = 0.71069$ Å) was employed and 52 reflections for tetrataenite [$a = 2.535(1)$ Å, $c = 3.583(1)$ Å, space group *P4/mmm*] were obtained in the 2θ range up to 53°, while 2405 reflections were taken for schreibersite [$a = 9.01737(18)$ Å, $c = 4.46044(15)$ Å, space group $I\bar{4}$] in the 2θ range up to 55°. These lattice constants can be compared with published data (Clarke and Scott 1980; Skála and Císařová 2005).

Fe, Ni, and Ge K-edge XAFS measurements were performed using beamline BL-9C in fluorescence mode, equipped with a Si (111) double-crystal monochromator at the Photon Factory, KEK, Tsukuba, Japan. The storage ring operation voltage was 2.5 GeV, and the electric current was 450 mA. X-ray energy calibration was performed by setting the copper metal pre-edge absorption peak to 8978.8 eV. A mirror was used to eliminate the higher harmonics. Then, an XAFS analysis was performed using XAFS93 and MBF93 programs (Maeda 1987; Wang et al. 2013; Yoshiasa et al. 1999). The EXAFS function $\chi(k)$ was extracted from measured spectrum using the standard procedure (Maeda 1987). For the quantitative analysis,

we used the Fourier filtering technique and a non-linear least-squares structure parameter fitting method with an analytical EXAFS formula by comparing the observed $\chi(k)_{exp}$ and calculated $\chi(k)_{calc}$. To obtain information regarding the structural parameters, we conducted parameter fitting using the analytical EXAFS formulae. Double-shell fitting was performed for the first and second nearest-neighbor distances for the body-centered cubic (BCC) iron foil. Reliability of the fit parameters, R, was determined as follows:

$$R = \Sigma \left| k_s^3 \chi(k_s)_{exp} - k_s^3 \chi(k_s)_{calc} \right| / \left| k_s^3 \chi(k_s)_{exp} \right|,$$

where R is the reliability between the experimental and calculated EXAFS functions, and was found to be less than 0.0084.

Results

Petrological and mineral chemistry characteristics

Original texture and mineral chemistry characteristics

The cross-section of the sample under an optical microscope shows an obvious Widmanstätten pattern. As expected, the backscattered SEM images also show a clear intergrowth structure of kamacite and tetrataenite (Fig. 1). Mineral kamacite, tetrataenite, and schreibersite were also observed (Figs. 1, 2). Tetrataenite mainly occurs at the boundary of the kamacite band. Their intergrowth shows structures from millimeter to submicrometer scales. The cloudy tetrataenite inside the kamacite bands formed plessite, as shown in Fig. 1d. Kamacite is lath-shaped, with 90° and 60° intersection angles appearing. Schreibersite shows a long-strip shape and less than 10 μm in width. The EDS mapping of
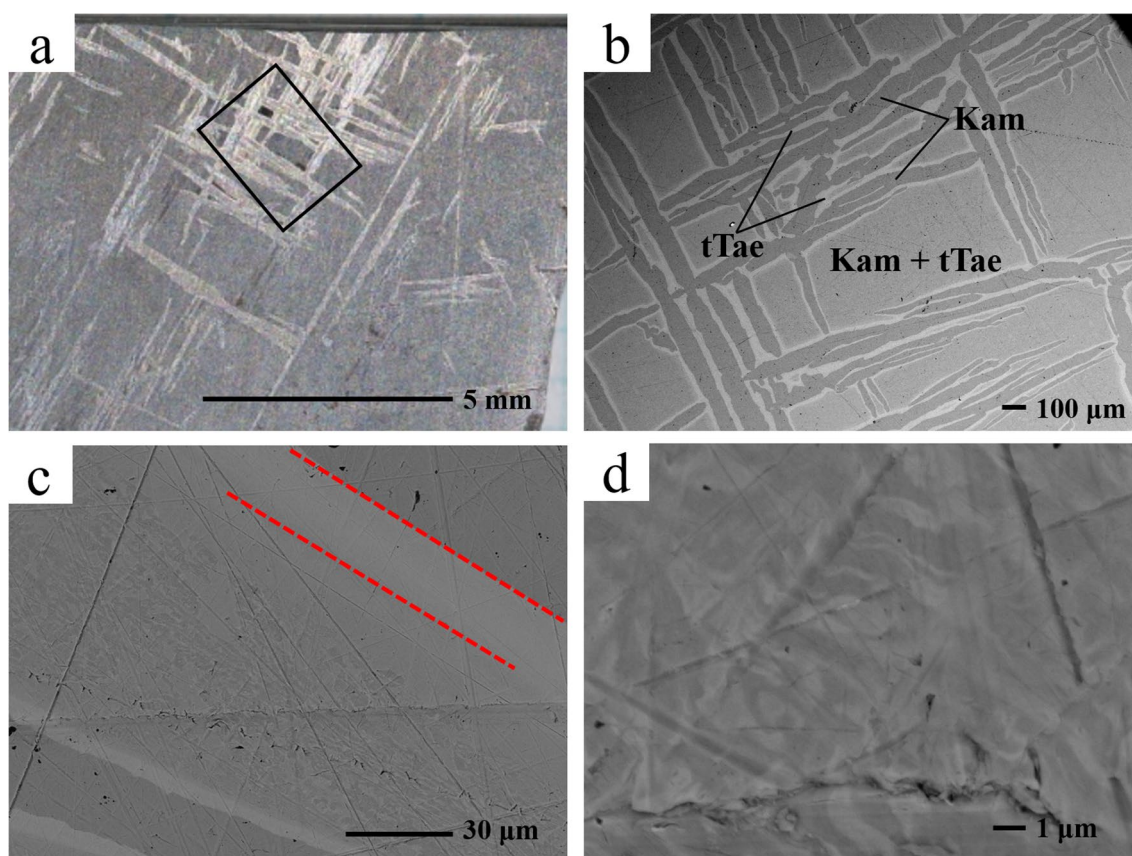

Fig. 1 **a** Photograph of NWA 859. Note that the Widmanstätten pattern could be seen by naked eyes, revealing intergrowth texture of kamacite and tetrataenite. **b**, **c**, **d** Backscattered electron (BSE) image of NWA 859, wherein **b** shows the corresponding texture at the position of rectangle area in (**a**), and **c** reveals the tiny pattern of the inside gradient in the kamacite band. Note that a pure tetrataenite wall exists on the phase boundary as marked between the dashed lines. **d** BSE image of submicron-sized kamacite and tetrataenite layer under high magnification. *Kam* Kamacite, *tTae* tetrataenite

Fig. 2 a Backscattered electron (BSE) image of schreibersite, which exists inside kamacite band in a rod like shape, as shown within the dashed line. **b** Elemental mapping for phosphorus distribution in the schreibersite grain in (**a**)
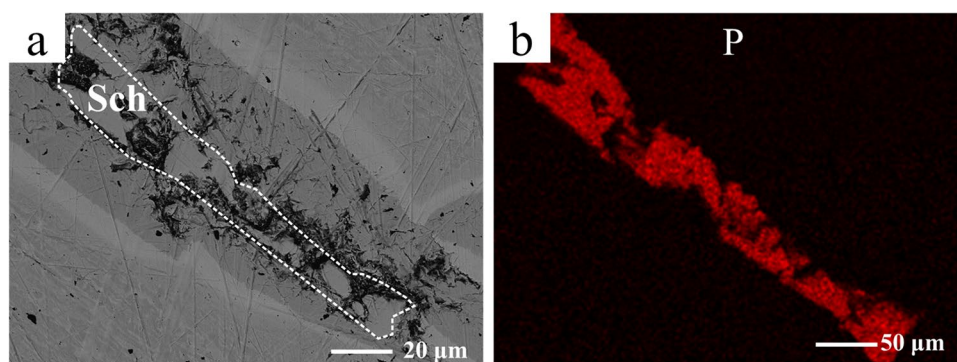
the phosphorus distribution was able to identify schreibersite from the kamacite surroundings (Fig. 2).

The well-studied bulk composition of NWA 859 shows that the Ni content is approximately 173 mg/g and has an extremely high Ge concentration, up to 2123 ppm as detected via Inductively coupled plasma mass spectrometry (ICP-MS) (D'Orazio and Folco 2003). The EDS analysis results show that the Ge content ranges from 0.21 to 0.92 wt.% in tetrataenite from both cloudy zone and tetrataenite lamella, and from 0.18 to 0.47 wt.% in kamacite lamella. Thus, the Ge content is highly concentrated in tetrataenite. Note that at a comparable concentration level, Ge is soluble in kamacite. The lowest Ni content detected in kamacite lamella is 5.07 wt.%, while the highest Ni content detected in tetrataenite is 45.37 wt.% from tetrataenite lamella. The remaining data detected from intergrowth region are spread throughout this composition range because of its intergrowth texture and the beam diameter of the EDS. The composition of schreibersite is summarized in Table 1. Moreover, tetrataenite has a typical chemical gradient crossing the Widmanstätten pattern and is enriched at the phase boundary.

Texture and chemical characteristics after nital etching

A piece of sample was etched with nital solution for 24 h. The surface was observed by SEM, showing a certain extent of separation of tetrataenite and kamacite. As shown in Fig. 3a, kamacite dissolved and formed cracks along the boundary in the intergrowth. The backscattered electron (BSE) image (Fig. 3b, c) of the sample surface reveals a loose fabric texture that consists of pure tetrataenite. The EDS results for such fabric areas show that the

Ni content is quite homogeneous with approximately 1 at% variation reaching 50.7 at%, which is the highest Ni content detected in the sample (Fig. 3c). The original tetrataenite and kamacite boundaries show segregation, and the coarse tetrataenite lamella elongates in several different directions. The Ni content in the tetrataenite lamella ranges from 43.60 to 49.44 at%. After 48 h of etching, another sample showed aggregation by magnetism with an exfoliated fine powder (Fig. 3d–e) that was several microns in size with a silver–gray metallic luster, as revealed under an optical microscope.

Phase identification and lattice parameter from XRD results

The X-ray powder diffraction at the Fe–Ni metal area results revealed a mixture of α-kamacite (BCC phase) and γ-like tetrataenite (FCC-like tetrataenite phase) without an intermediate composition. Figure 4 shows the diffraction pattern and plane indices of kamacite and tetrataenite. The signatures at 44.62°, 64.84°, 82.23°, and 98.68° 2θ indicate α-kamacite, while the signatures at 43.69°, 50.83°, 74.8°, and 90.72° 2θ indicate γ-tetrataenite. Combined with a calculation based on the least-squares method, we determined that the BCC kamacite has a lattice parameter of $a = 2.871(2)$ Å, and the FCC-like tetrataenite has a lattice parameter of $a = 3.590(2)$ Å. The results of the Ni metal reagent show a lattice parameter of $a = 3.526(1)$ Å and Fe metal reagent of $a = 2.864(1)$ Å. The bonding distances were calculated using their coordination numbers, as summarized in Table 2.

The X-ray single-crystal diffraction experiments indicated that tetrataenite has a tetragonal structure with

Table 1 Composition of schreibersite in NWA 859

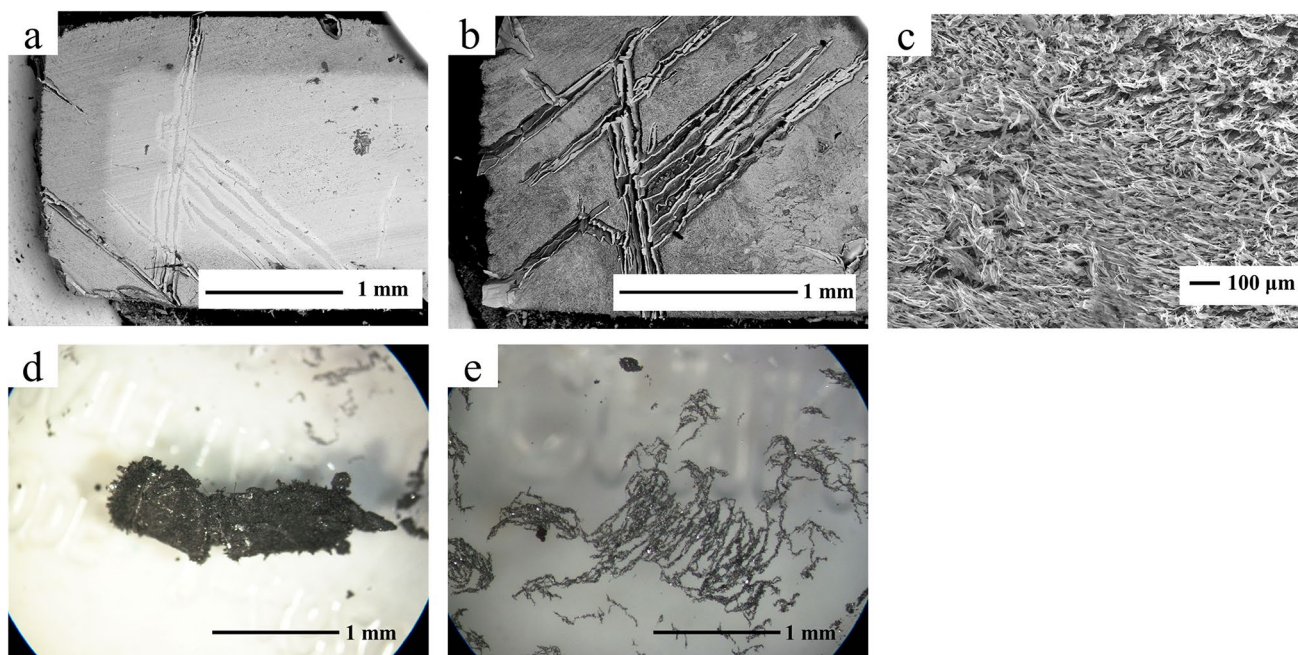| No	Atom (%)							Mass (%)						
	P	Fe	Co	Ni	Ga	Ge	Total	P	Fe	Co	Ni	Ga	Ge	Total
1	24.98	32.47	0.22	42.19	0.08	0.06	100	15.64	36.64	0.26	50.05	0.11	0.09	102.79
2	24.95	32.59	0.23	42.07	0.11	0.05	100	15.61	36.76	0.28	49.89	0.16	0.08	102.77
3	25.38	32.18	0.23	42.00	0.15	0.06	100	15.89	36.32	0.27	49.83	0.22	0.08	102.61

Fig. 3 **a** Backscattered electron (BSE) image of a piece of NWA 859 after etching for 24 h, **b**, **c** 48 h. Note the fiber like tetrataenite residual on the main body. **d** Optical microscope image of the main body. **e** Optical microscope image of powders exfoliated from etched main body, wherein the powder mainly contains schreibersite and tetrataenite

Fig. 4 Powder diffraction pattern of kamacite and tetrataenite in NWA 859 sample. *K* Kamacite, *T* Tetrataenite, Fe_3O_4 Magnetite. The plain indices for kamacite and tetrataenite for each peak were marked at the characteristic peaks
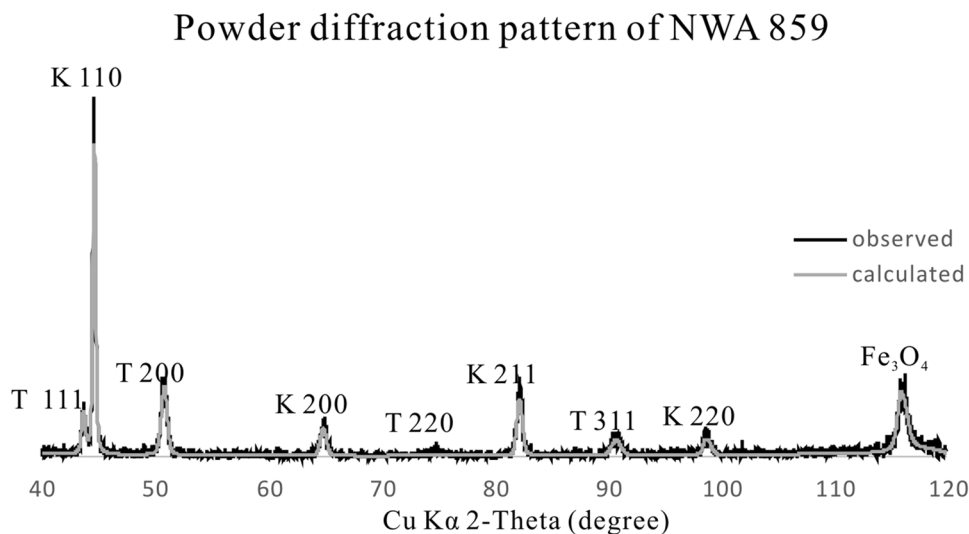
$a = 2.535(1)$ Å, ($\sqrt{2}a = 3.585(1)$ Å), and $c = 3.583(1)$ Å, revealing only minor differences from the FCC lattice parameter, as shown in Fig. 5. The values of the lattice parameters for tetrataenite are consistent with the published values of $a = 2.533(2)$ Å and $c = 3.582(2)$ Å (Clarke and Scott 1980). Note that the relationship between the composition and lattice constant is already known for the Fe–Ni solid solution system (Swartzendruber et al. 1991).

Thus, the lattice parameters of 2.871(2) Å for kamacite and 3.590(2) Å for tetrataenite indicate Ni contents of approximately 5.00 at.% and 50.00 at.%, respectively. These results are in good agreement with those of the chemical analyses. The error values of the calculated lattice parameters in parentheses were acquired from the full width at half maximum in different phases according to the error value from the PDXL regression.

Table 2 Bonding distances and structural parameters determined by extended X-ray absorption fine structure (EXAFS) and X-ray diffraction (XRD) methods

Sample	Coordination number	Distance (EXAFS)	Debye–Waller factor (EXAFS)	R-factor (EXAFS)	Distance (XRD)
Ge-(Ni,Fe) in NWA859 tetrataenite	12	2.524 (5)	0.0185 (5)	0.0084	–
Ge–Ge in pure diamond-type	4	2.471 (4)	0.0062 (3)	0.0061	2.450 (1)
Ni-(Ni,Fe) in NWA859 tetrataenite	12	2.5170 (13)	0.00960 (10)	0.0021	–
Ni–Ni in pure FCC metal	12	2.4880 (9)	0.00737 (7)	0.0018	2.494 (1)
Fe-(Ni,Fe) in NWA859 tetrataenite	12	2.534 (3)	0.0093 (3)	0.0042	–
(Ni,Fe)–(Ni,Fe) in NWA 859 tetrataenite ($Fe_{50}Ni_{50}$)	12	–	–	–	2.535 (1)
(Fe,Ni)–(Fe,Ni) in NWA 859 kamacite ($Fe_{0.95}Ni_{0.05}$)	8 + 6	–	–	–	2.486 (2) 2.870 (2)
Fe–Fe in pure BCC metal	8 + 6	2.4967 (16) 2.886 (3)	0.00659 (12) 0.0118 (4)	0.0008	2.480 (1) 2.864 (1)
Fe–Fe in FCC austenite (Fe,C)[a]	12	–	–	–	2.52–2.53

Fe-Fe in face-centered cubic (FCC) austenite (Fe, C) obtained from Nascimento et al. (2009)

Fig. 5 Lattice structure of $L1_0$ tetrataenite. Lattice constant $a = 2.535(1)$ Å and $c = 3.583(1)$ Å. The yellow spheres and gray spheres represent Fe and Ni atoms, respectively. The unit cells in broken and solid lines represent the taenite cell and the tetrataenite cell, respectively. The structure was modified based on figures drawn by VESTA (Momma and Izumi 2011)
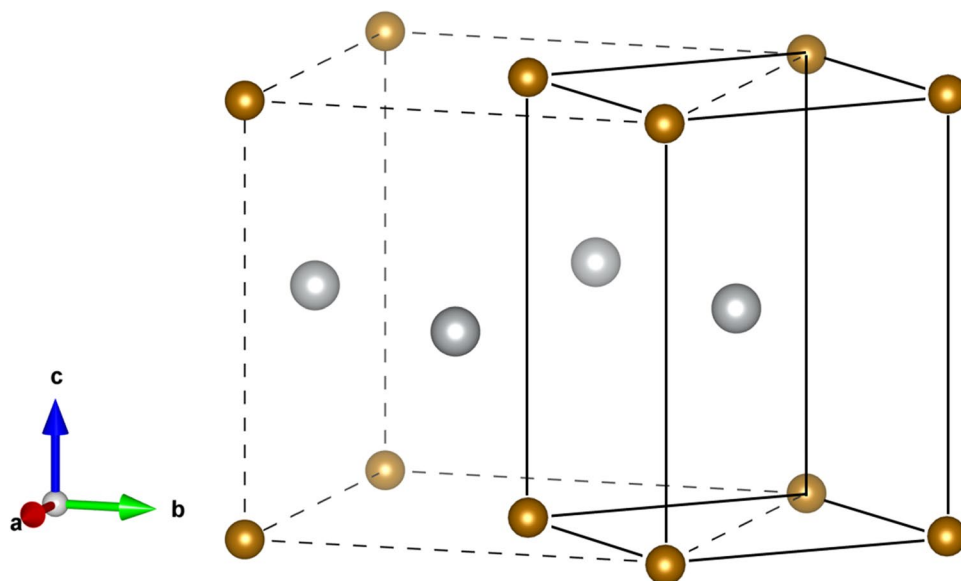
XAFS study

XANES results

The XANES spectra patterns were obtained for Fe, Ni, and Ge in the tetrataenite of NWA 859 as well as standard Fe foil, Ni foil, and Ge metal, as shown in Fig. 6. The patterns of the Fe K-edge show that Fe in NWA 859 tetrataenite has a higher pre-edge height, located at approximately two-thirds of the first peak height, compared with both Fe foil and high-pressure hexagonal closest packed (HCP) ε-Fe under 42 GPa with a pre-edge at approximately one-third of the first peak height (Fig. 6a). This is a distinguishable feature, suggesting that it is not a BCC structure. The Fe K-edge XANES

spectrum for HCP ε-Fe at 42 GPa and 300 K were measured in transmission mode using a diamond anvil cell (Yoshiasa et al. 2009). As well, the first peak shape of Fe in NWA 859 tetrataenite is quite broad compared with the BCC Fe foil. The shape of the Fe XANES spectrum for the tetrataenite in NWA 859 is more similar to that for ε-Fe, wherein Fe has a coordination number of 12.

The XANES patterns of Ni K-edge show that Fe in the NWA 859 tetrataenite has a similar pre-edge and peak relationship compared to the Ni foil (Fig. 6b). Attenuation of the XAFS signal for NWA 859 tetrataenite occurs as a result of an increase in positional displacement due to the coordination of Fe with a different element. A comparison between the first derivative spectra of Ni XANES spectra (Fig. 7a) for
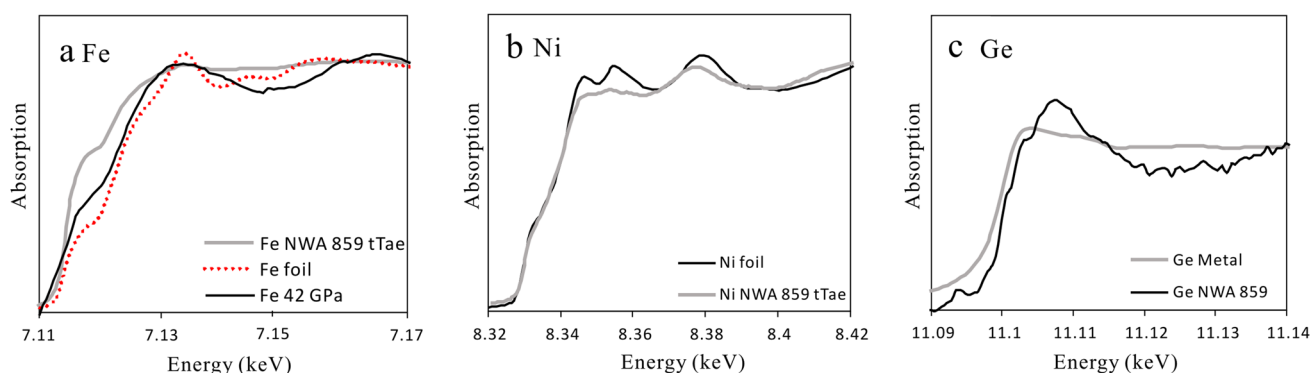
Fig. 6 Fe K-edge X-ray absorption near-edge structure (XANES) spectra of **a** Fe foil in Fe high-pressure phase (Yoshiasa et al. 2009), and tetrataenite (tTae) and **b** Ni foil and tetrataenite in NWA 859. **c** Ge K-edge XANES spectra of Ge metal and Ge in tetrataenite in NWA 859
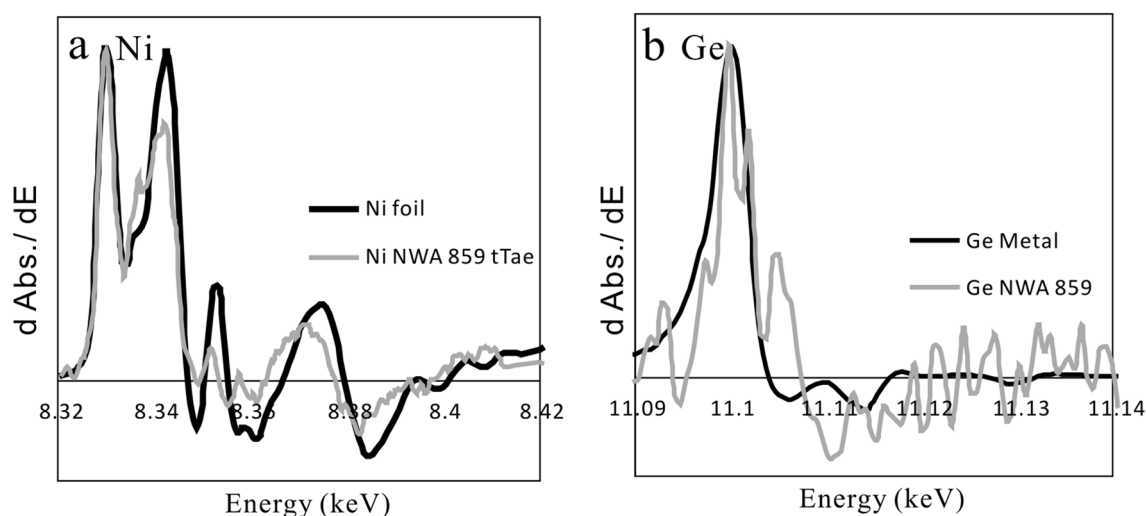

Fig. 7 **a** First derivative spectra of **a** Ni foil and tetrataenite and **b** Ge metal and Ge in tetrataenite of NWA 859

Ni foil and tetrataenite in NWA 859 confirms that there is no chemical shift for Ni metal in tetrataenite. Furthermore, the Ge spectra were compared with Ge metal, revealing different peak top positions and shapes, as shown in Fig. 6c. The first peak of Ge in NWA 859 is much broader than that of the Ge metal, which suggests that Ge has formed a local structure compared with the common diamond-type Ge. Moreover, a comparison between the first derivative spectra for Ge metal and tetrataenite in NWA 859 confirms that the Ge in tetrataenite has almost no chemical shift from the Ge metal.

EXAFS results

Lattice parameter and local structure information were obtained through EXAFS fitting, and the results are listed in Table 2, wherein the Debye–Waller factor represents the mean square of the relative displacement between the absorbing and backscattering atoms. Figure 8 shows the

Fourier transform of Fe, Ni, and Ge K-edge EXAFS spectra for tetrataenite in NWA 859.

Discussion

Local structure of Fe, Ni, and Ge in NWA 859 meteorite

The EXAFS analyses of NWA 859 and single-crystal diffraction of tetrataenite reveal that tetrataenite has a near-FCC tetragonal structure with 12 nearest-neighboring Ni, Fe, and Ge atoms at distances $r_{Ni-(Ni, Fe)} = 2.5170(13)$ Å, $r_{Fe-(Ni, Fe)} = 2.534(3)$ Å and $r_{Ge-(Ni, Fe)} = 2.524(5)$ Å, which are quite similar. Ge becomes a substitution atom, replacing Ni or Fe in the tetrataenite with a coordination number of 12. Thus, we suggest that the NWA 859 meteorite was formed under higher pressure, which is different than typical
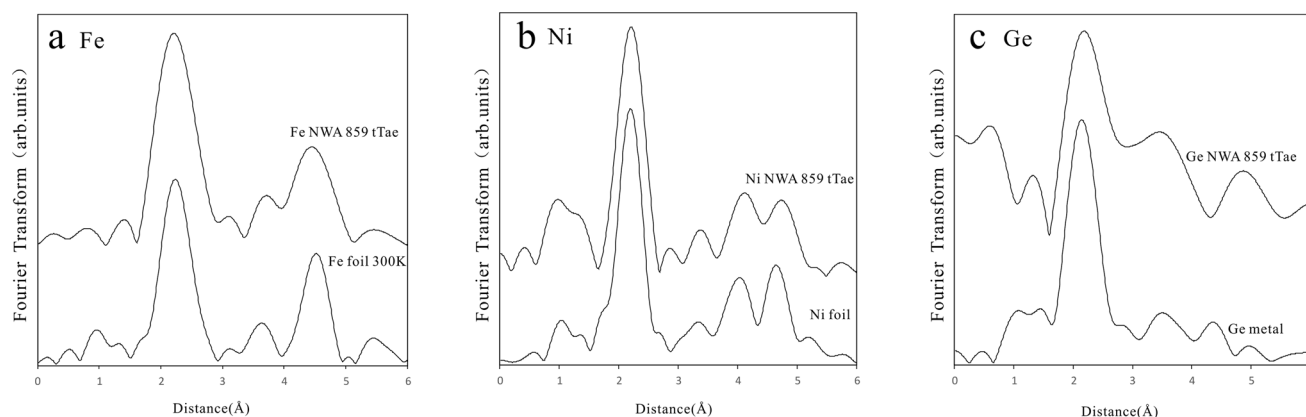
Fig. 8 **a** Fourier transform of extended X-ray absorption fine structure (EXAFS) for **a** Fe K-edge in Fe foil and tetrataenite in NWA 859, **b** Ni K-edge in Ni foil and tetrataenite in NWA 859, and **c** Ge K-edge in Ge metal and tetrataenite in NWA 859

iron meteorites. The formation pressure at the center of typical metallic objects with radii of approximately 50–200 km was calculated to range from 0.2 to 3.1 kbar (Schwarcz et al. 1975). Moreover, the iron meteorite Butler, which is believed to be chemically related to NWA 859, has an extremely high Ge concentration (2000–2300 µg/g). At the same time, magmatic trends (such as negative Ir–Au and Ir–As trends) in both Butler and NWA 859 could not be recognized (Wasson 2011). In addition, Ga and Ge are volatile siderophile elements that behave similarly in iron meteorites. Particularly, Ge is concentrated in NWA 859 (approximately 1 order of magnitude higher than other iron meteorites) and Ga is only slightly rich in the same order of magnitude as seen in other iron meteorites. The non-magmatic chemical characteristics suggest that it was not originate from the core of its parent body. At the same time, we inferred that the high Ge content of NWA 859 was caused by the Ge rich resource region in the parent body, in which Ge entered

the tetrataenite structure with a 12 coordination under high pressure. The high-pressure Ge structure and non-magmatic chemical characteristic of NWA 859 suggest that it formed by some shock compression event happened on the parent body.

Texture formation mechanism interpreted with the Fe–Ni phase diagram

The size of the mineral grains and texture are indicators of the thermal history in the meteorite parent bodies. Iron meteorites form a Widmanstätten pattern during a long cooling process with oriented kamacite and tetrataenite lamellae (Fig. 1). As the texture of the etched sample surface shows tiny fabric tetrataenite (Fig. 3c), the original sample is likely a mixture of two different phases. The chemical gradient of tetrataenite found in the EDS analysis formed by tetrataenite and kamacite mixing in different proportions (Fig. 9). Thus,
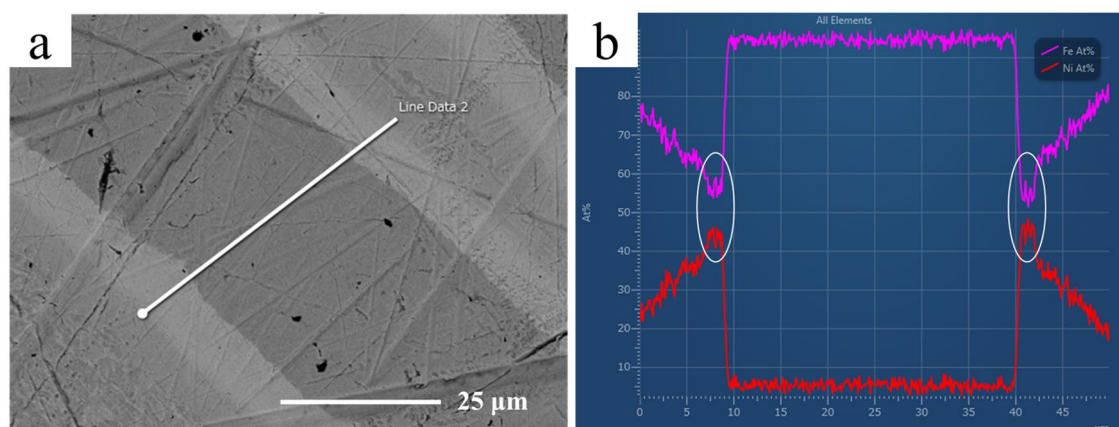

Fig. 9 **a** Backscattered electron (BSE) image of unetched NWA 859. **b** Energy-dispersive spectra (EDS) line analysis of the line marked in (**a**). The oval marks show that the gradient stopped changing
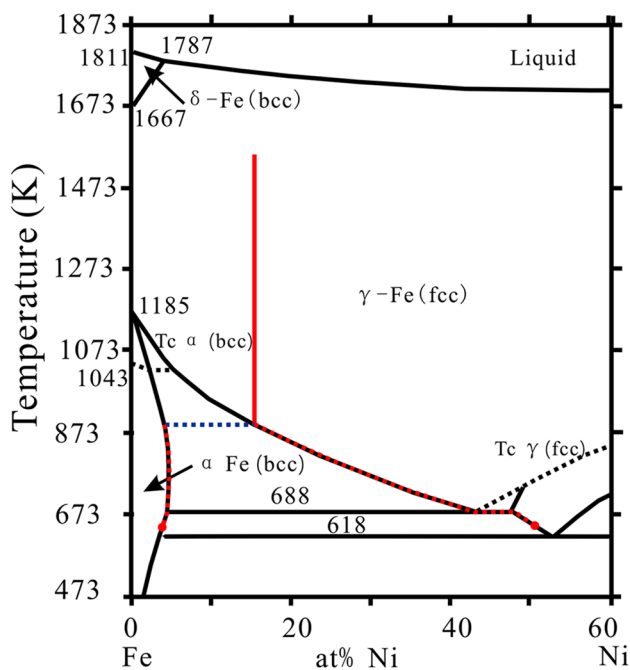
Fig. 10 Fe–Ni phase diagram modified from Cacciamani et al. 2006. *Tc* Currie temperature. The red line represents the homogeneous host phase. The blue dotted line shows when the crystallization of kamacite began. The red dotted lines represent kamacite and taenite phase separation with decreasing temperature and the red filled circles marking the end of the dotted red lines represent the end of the crystallization process

we inferred that the composition of tetrataenite grains is actually homogeneous. The chemical gradient was acquired as a mixture of extremely tiny kamacite and tetrataenite, which produced a wide chemical range, as shown in Fig. 9.

Because the composition and grain size growing with temperature variation followed the Fe–Ni phase diagram, the cooling path could be inferred from the detected mineral composition in NWA 859. Starting with a bulk composition of 17.3 wt.% Ni (D'Orazio and Folco 2003), as temperature decreases, kamacite nucleates at approximately 883 K when martensite (BCC) forms. Thus, the red vertical line represents the homogeneous host FCC phase, the dotted blue horizontal line represents when the phase separation started, and the red dotted lines along the eutectic lines represent the crystallization process of the kamacite and taenite phases (Fig. 10). The diffusion rate difference in the two alloys limited the growth of kamacite in taenite (Dauphas 2007), thereby causing a chemical gradient to form a characteristic M-shaped profile in taenite, as shown in Fig. 9. The cooling crystallization process follows the route marked in the phase diagram (Fig. 10), which was suggested by thermodynamic calculations and confirmed via experimental investigations (Cacciamani et al. 2006). As the etched cloudy zone shows a composition of approximately Fe50–Ni50, which fits with

tetrataenite, when the temperature decreased below 623 K, the cloudy tetrataenite was believed to be formed by magnetically induced spinodal decomposition of the metastable tetrataenite during slow cooling (Albertsen et al. 1983). Reuter et al. (1989) suggested that tetrataenite is thermodynamically stable at 298.15 K. Since tetrataenite only appears inside taenite phases, but is not observed in kamacite (stable BCC) and taenite boundary, this indicates that the tetrataenite is merely metastable under true thermodynamic equilibrium at room temperature (Howald 2003).

A highly oriented Fe–Ni structure in a diffusion-controlled process occurred as tetrataenite in the cloudy zone. Cloudy tetrataenite has a lattice parameter of $a = b = 2.535(1)$, $c = 3.583(1)$, as detected by single-crystal diffraction. Converting to the face-centered structure, the unit cell has a parameter of $a = 2.535(1)$ Å $[\sqrt{2}a = 3.585(1)$ Å$]$ and $c = 3.583(1)$ Å, wherein the c-axis is just reduced a little compared with the cubic FCC structure. The CuAu $L1_0$ structure is a tetragonal distortion of the FCC structure, which becomes shorter in the c-axis direction with structural stabilization (Bayliss 1990). Therefore, only tetrataenite developing under a long-time slow cooling history could form the $L1_0$ structure. As the metal phase has a higher thermal conductivity than silicate crusts, the slow cooling history of the metallic core usually represents large parent bodies with silicate mantle that give global heat dissipation slowly.

Conclusions

The local structures of Fe, Ni, and Ge in the lattice of tetrataenite were acquired using the XAFS method with high precision. EXAFS is an effective method for studying the local structure of iron meteorites as it provides consistent results of the lattice parameter with XRD.

A new local structure of Ge-(Ni, Fe) was discovered in extraterrestrial material. Thus, it has been proven that Ge can serve as a substitution atom of Ni or Fe in tetrataenite, forming a stable tetragonal structure at approximately 688–618 K. The iron meteorite NWA 859 possibly formed through a shock event on the surface of parent body rather than being a remnant of an asteroid's inner core. The formation condition and thermal history of NWA 859 were inferred from the texture and composition characteristics combined with an evaluation of the phase diagram.

References

Albertsen JF, Nielsen HP, Buchwald VF (1983) On the fine structure of meteoritical taenite/tetrataenite and its interpretation. Phys Scr 27:314–320. https://doi.org/10.1088/0031-8949/27/4/015

Bayliss P (1990) Revised unit-cell dimensions, space group, and chemical formula of some metallic minerals. Can Mineral 28:751–755

Cacciamani G, De Keyzer J, Ferro R, Klotz UE, Lacaze J, Wollants P (2006) Critical evaluation of the Fe–Ni, Fe–Ti and Fe–Ni–Ti alloy systems. Intermet 14:1312–1325. https://doi.org/10.1016/j.intermet.2005.11.028

Clarke RS, Scott ERD (1980) Tetrataenite—ordered FeNi, a new mineral in meteorites. Am Mineral 65:624–630

Cressey G, Dent AJ, Dobson B, Evans A, Greaves GN, Henderson CMB, Hutchinson R, Jenkins RN, Thompson SP, Zhu R (1989) Atomic environments in iron meteorites using EXAFS (Extended X-ray absorption fine structure). Interstellar Dust 135:455

Dauphas N (2007) Diffusion-driven kinetic isotope effect of Fe and Ni during formation of the Widmanstätten pattern. Meteorit Planet Sci 42:1597–1613. https://doi.org/10.1111/j.1945-5100.2007.tb00593.x

D'Orazio M, Folco L (2003) Chemical analysis of iron meteorites by inductively coupled plasma-mass spectrometry. Geostand Geoanal Res 27:215–225. https://doi.org/10.1111/j.1751-908X.2003.tb00723.x

Howald RA (2003) The thermodynamics of tetrataenite and awaruite: a review of the Fe–Ni phase diagram. Metall Mater Trans A 34:1759–1769

Lovering JF, Nichiporuk W, Chodos A, Brown H (1957) The distribution of gallium, germanium, cobalt, chromium, and copper in iron and stony-iron meteorites in relation to nickel content and structure. Geochim Cosmochim Acta 11:263–278. https://doi.org/10.1016/0016-7037(57)90099-6

Maeda H (1987) Accurate bond length determination by EXAFS method. J Phys Soc Jpn 56:2777–2787. https://doi.org/10.1143/JPSJ.56.2777

Momma K, Izumi F (2011) VESTA 3 for three-dimensional visualization of crystal, volumetric and morphology data. J Appl Crystallogr 44:1272–1276. https://doi.org/10.1107/S0021889811038970

Nascimento FC, Foerster CE, Silva SLRd, Lepienski CM, Siqueira CJdM, Alves Junior C (2009) A comparative study of mechanical and tribological properties of AISI-304 and AISI-316 submitted to glow discharge nitriding. Mater Res 12:173–180. https://doi.org/10.1590/S1516-14392009000200011

Reuter K, Williams DB, Goldstein J (1989) Determination of the Fe–Ni phase diagram below 400 C. Metall Trans A 20:719–725

Schaudy R, Wasson JT, Buchwald VF (1972) The chemical classification of iron meteorites. VI. A reinvestigation of irons with Ge concentration lower than 1 ppm. Icarus 17:174–192. https://doi.org/10.1016/0019-1035(72)90053-X

Schwarcz HP, Scott SD, Kissin SA (1975) Pressures of formation of iron meteorites from sphalerite compositions. Geochim et Cosmochim Acta 39:1457–1466. https://doi.org/10.1016/0016-7037(75)90147-7

Scott ERD (1972) Chemical fractionation in iron meteorites and its interpretation. Geochim et Cosmochim Acta 36:1205–1236. https://doi.org/10.1016/0016-7037(72)90046-4

Skála R, Císařová I (2005) Crystal structure of meteoritic schreibersites: determination of absolute structure. Phys Chem Miner 31:721–732. https://doi.org/10.1007/s00269-004-0435-6

Swartzendruber LJ, Itkin VP, Alcock CB (1991) The Fe–Ni (iron-nickel) system. J Phase Equilibria 12:288–312. https://doi.org/10.1007/BF02649918

Takahashi Y, Shimizu H, Kagi H, Yoshida H, Usui A, Nomura M (2000) A new method for the determination of CeIII/CeIV ratios in geological materials; application for weathering, sedimentary and diagenetic processes. Earth Planet Sci Lett 182:201–207. https://doi.org/10.1016/S0012-821X(00)00250-8

Wai CM, Wasson JT (1979) Nebular condensation of Ga, Ge and Sb and the chemical classification of iron meteorites. Nature 282:790–793. https://doi.org/10.1038/282790a0

Wang L, Yoshiasa A, Okube M, Hiratoko T, Hu Y, Arima H, Sugiyama K (2013) Local structure of iron in tektites and natural glass: an insight through X-ray absorption fine structure spectroscopy. J Mineral Petrol Sci 108:130212. https://doi.org/10.2465/jmps.130212

Wasson JT (1967) The chemical classification of iron meteorites: I. A study of iron meteorites with low concentrations of gallium and germanium. Geochim Cosmochim Acta 31:161–180. https://doi.org/10.1016/S0016-7037(67)80043-7

Wasson JT (1970) The chemical classification of iron meteorites: IV. Irons with Ge concentrations greater than 190 ppm and other meteorites associated with group I. Icarus 12:407–423. https://doi.org/10.1016/0019-1035(70)90009-6

Wasson JT (2011) Relationship between iron-meteorite composition and size: compositional distribution of irons from North Africa. Geochim Cosmochim Acta 75:1757–1772. https://doi.org/10.1016/j.gca.2010.12.017

Wasson JT, Kimbeblin J (1967) The chemical classification of iron meteorites—II. Irons and pallasites with germanium concentrations between 8 and 100 ppm. Geochim Cosmochim Acta 31:2065–2093. https://doi.org/10.1016/0016-7037(67)90143-3

Xue S, Yang YL, Hall GS, Herzog GF (1997) Germanium isotopic compositions in Canyon Diablo spheroids. Geochim Cosmochim Acta 61:651–655. https://doi.org/10.1016/S0016-7037(96)00363-8

Yang J, Goldstein JI, Scott ERD (2007) Iron meteorite evidence for early formation and catastrophic disruption of protoplanets. Nat 446:888–891. https://doi.org/10.1038/nature05735

Yoshiasa A, Nagai T, Ohtaka O, Kamishima O, Shimomura O (1999) Pressure and temperature dependence of EXAFS Debye-Waller factors in diamond-type and white-tin-type germanium. J Synchrotron Radiat 6:43–49. https://doi.org/10.1107/S0909049598011947

Yoshiasa A, Ohtaka O, Sakamoto D, Andrault D, Fukui H, Okube M (2009) Pressure and compositional dependence of electric conductivity in the $(Mg_{1-x}Fe_x)_{1-\delta}O$ ($x = 0.01–0.40$) solid-solution. Solid State Ion 180:501–505. https://doi.org/10.1016/j.ssi.2008.10.012